Surface aerosol radiative forcing derived from collocated ground-based radiometric observations during PRIDE, SAFARI, and ACE-Asia

Richard A. Hansell, Si-Chee Tsay, Qiang Ji, K. N. Liou, and Szu-Cheng Ou

An approach is presented to estimate the surface aerosol radiative forcing by use of collocated cloud-screened narrowband spectral and thermal-offset-corrected radiometric observations during the Puerto Rico Dust Experiment 2000, South African Fire Atmosphere Research Initiative (SAFARI) 2000, and Aerosol Characterization Experiment–Asia 2001. We show that aerosol optical depths from the Multiple-Filter Rotating Shadowband Radiometer data match closely with those from the Cimel sunphotometer data for two SAFARI-2000 dates. The observed aerosol radiative forcings were interpreted on the basis of results from the Fu–Liou radiative transfer model, and, in some cases, cross checked with satellite-derived forcing parameters. Values of the aerosol radiative forcing and forcing efficiency, which quantifies the sensitivity of the surface fluxes to the aerosol optical depth, were generated on the basis of a differential technique for all three campaigns, and their scientific significance is discussed.

OCIS codes: 120.5630, 120.0280, 120.4640, 120.6810, 280.1100, 290.1090.

1. Introduction

The quantification of the surface aerosol radiative forcing (SARF) and the minimization of its uncertainty remain the two primary goals in today's studies of radiative effects of aerosols. A major global effort given toward these areas is the aerosol robotic network (AERONET) program. Under the initiative and guidance of the National Aeronautics and Space Administration (NASA) Goddard Space Flight Center,[1] the AERONET uses eight-channel sunphotometers, manufactured by Cimel Electronique, at measurement sites all over the world to derive aerosol optical properties to facilitate the estimation of SARF on the basis of observations. The inversion routines of Nakajima *et al.*[2] and from AERONET[3] are used to retrieve aerosol optical depths, single-scattering albedos, scattering phase functions, asymmetry parameters, and indices of refraction.

There have been numerous efforts to estimate SARF. Most recently Schafer *et al.*[4] showed that, by use of the sunphotometer to retrieve aerosol optical depths, τ_a, along with observed surface flux data from field campaigns in Brazil and south central Africa, aerosol radiative forcing efficiencies due to smoke particulates were determined to be -145 $(W/m^2)/\tau_a$ and -210 $(W/m^2)/\tau_a$, respectively, for the range of instantaneous solar zenith angles (θ_o) between 25° and 35°. Maximum reductions in surface flux of the order of 337 $(W/m^2)/\tau_a$, for $\theta_o = 31°$ were observed for the heaviest smoke conditions ($\tau_a = 3.0$) in Brazil. The difference in the aerosol attenuation of flux between both sites is attributed to the variable composition of the fire-source materials and the type of combustion. Christopher *et al.*[5] used retrieved aerosol optical depth from half-hourly Geostationary Operational Environmental Satellite (GOES-8) imager data as well as collocated surface fluxes measured by NASA's Surface Measurements for Atmospheric Radiative Transfer system during the Puerto Rico Dust Experiment (PRIDE) to estimate the top-of-the-atmosphere aerosol radiative forcing and SARF. On the basis of on a mean τ_a value of 0.26, the daytime average SARF and associated standard deviation

R. A. Hansell (rhansell@atmos.ucla.edu), K. N. Liou, and S.-C. Ou are with the Department of Atmospheric Sciences, University of California, Los Angeles, Los Angeles, California 90095-1565. S.-C. Tsay and Q. Ji are with Goddard Space Flight Center, NASA, Greenbelt, Maryland.

Received 1 November 2002; revised manuscript received 21 April 2003.

0003-6935/03/275533-12$15.00/0

over a period from 28 June to 26 July 2000 were found to be -18.13 and 15.81 W/m^2, respectively. Data from the first field phase of the Indian Ocean Experiment have also been studied for estimating the SARF over the Indian Ocean.[6,7] It was shown that, for a soot-laden marine region south of India, a 0.1 change in τ_a leads to a -4.0 ± 0.08 W/m^2 change in the 0.4–0.7-μm surface flux. Differences in the reported forcings are due to the corresponding changes in τ_a as identified in Schafer *et al.*,[4] whereas the monthly mean forcing is obtained by multiplication of the efficiencies by observed τ_a.

This paper focuses on the quantification of SARF by use of radiometric and sunphotometer data from PRIDE 2000,[5] South African Fire Atmosphere Research Initiative[8] (SAFARI) 2000, and Aerosol Characterization Experiment–Asia[9] (ACE-Asia) 2001 and radiometric measurements at the University of California at Los Angeles (UCLA) surface site. The focus of PRIDE is the study of the radiative, microphysical, and transport properties of dust from the Saharan Desert at the Roosevelt Road Naval facility in Puerto Rico. Similarly, the goals of SAFARI and ACE-Asia are to study aerosol properties at and around Skukuza, South Africa, and Dunhuang, China, respectively. The aerosols over these areas were generated from local biomass burnings, biological and industrial sources, sand blowing over desert, and urbanized sources.

The scientific objectives of the studies reported in this paper are as follows. First, spectral measurements from the Multiple-Filter Rotating Shadowband Radiometer (MFRSR) and the Cimel sunphotometer and surface fluxes from broadband radiometers are calibrated and processed. The time series of τ_a and surface radiative fluxes are generated for selected dates during each field campaign. The retrieved τ_a from the MFRSR and the sunphotometer are then intercompared. Similar comparisons of τ_a from these two instruments were reported by Augustine and Medina[10] and Jin *et al.*[11] Because the MFRSR's sampling frequency is approximately 60 times greater than that of the Cimel sunphotometer, we chose to use the MFRSR data to determine the SARF to produce statistically meaningful results.

Second, because clouds were prevalent during PRIDE 2000, it is necessary to develop an effective cloud-screening scheme to remove effects of cloud bias in the retrieved aerosol properties and estimates of SARF. The magnitude of thermal offsets in the UCLA pyranometer data is also evaluated, and an empirical correction method to enhance the accuracy of the measured downward solar flux is developed. Finally, by use of the irradiance data from collocated broadband radiometers along with the time series of retrieved τ_a, quantitative estimates of the SARF are made for each campaign. Two parameters are derived. The first is the aerosol radiative forcing, which is a measure of the radiative effects of the aerosol. The second is the aerosol forcing efficiency, which is defined as the derivative of surface flux with respect to the aerosol optical depth. In this study we directly determine SARF parameters from measurements, and the results can be used as a tool for validating satellite-retrieved aerosol radiative forcing. Knowledge of the regionally estimated SARF parameters will help the study of global climate change and improve the aerosol parameterizations in radiative transfer models.

The arrangement of this paper is as follows. Section 2 discusses the primary instrumentation used in the study, including a brief introduction of the UCLA surface radiometric site. Section 3 describes the cloud-removal procedure, the cross-calibration scheme that uses the Cimel sunphotometer, and the τ_a retrieval scheme subject to the correction of Rayleigh scattering and ozone absorption. In Section 4, estimates of surface aerosol radiative forcing and forcing efficiency are presented. Also included in this section are turbidity coefficients and shaping factors determined from Angstrom's empirical relation for SAFARI and model comparisons of the predicted SARF with the observed SARF by use of the Fu–Liou radiative transfer code.[12] Finally, a summary is given in Section 5.

2. Instrumentation

The primary instrumentation used in this study includes the MFRSR and the Total Solar Pyranometer (TSP), the TSP-700, from Yankee Environmental Systems (YES), the Cimel Electronique sunphotometer (CE-318), and Epply's precision spectral pyranometer (PSP). Both the MFRSR and the CE-318 contain narrowband visible and near-infrared interference filters, each 10-nm full width half-maximum (FWHM). The MFRSR channels cover the following wavelengths: 0.41, 0.49, 0.61, 0.67, 0.86, and 0.94 μm. In addition, it contains one unfiltered broadband silicon pyranometer whose spectral response is 0.30–1.10 μm. The MFRSR employs an automated rotating shadowband to make simultaneous measurements of the total, diffuse, and direct-normal components of the solar spectral irradiance. MFRSR calibration, performed at the YES laboratory, involves evaluating the angular, spectral, and absolute responses for each channel. Instrument output is subject to uncertainty owing to variations in the ambient temperature, which has been shown by a recent Atmospheric Radiation Measurement Program study[13] (May 2000) to be in the range of 1%–2% per 1-K change in sensor-head temperature. Another uncertainty is the positioning error in the shadowband, which could lead to a positive bias in diffuse irradiance, and, consequently, the total component would be underestimated. Shadowband errors occurred at the start of PRIDE, so these data were rejected in the following analysis.

The Cimel sunphotometer contains the following channels: 0.34, 0.38, 0.44, 0.50, 0.67, 0.87, 0.93, and 1.02 μm. It is designed to perform automated direct solar and sky-scanning spectral radiometric measurements every 15 min throughout the day. Sky-scanning channels are calibrated by use of the NASA Goddard Space Flight Center's 2-m integrating

Table 1. Primary Instruments and Measurements for PRIDE, SAFARI, and ACE-Asia

Instrument	Parameters Measured or Derived	Spectral Characteristics	Accuracy
Eppley PSP	Downward short-wave irradiance	Broadband (0.2–4.0 μm)	±5% (±10 W/m^2)[a]
YES MFRSR	Narrowband direct, diffuse and global southwest irradiance/τ_a, and column water vapor and ozone	Center wavelengths (0.41, 0.49, 0.61, 0.67, 0.86, and 0.94 μm)	1% (Langley calibration) with ~1% for τ_a retrieval
AERONET Cimel Sunphotometer	Narrowband direct, diffuse radiance/τ_a, single-scattering albedo, asymmetry parameter, and volume size distribution	Center wavelengths (0.34, 0.38, 0.44, 0.50, 0.67, 0.87, 0.93, and 1.02 μm)	Sky radiance measurements (1%–3%)[b] Direct radiance measurements (≤1%)[c]

[a]When calibrated within 1 yr to the World Radiometric Reference.
[b]Reported accuracy of 2-m integrating sphere.[1]
[c]Reported accuracy for visible wavelengths, $\lambda > 0.44$ μm used in study.

sphere, and the direct solar scans are compared with a reference instrument calibrated with Mauna Loa Observatory Langley. The measured uncertainty in the retrieved τ_a is estimated to be ~0.01–0.02.[1] Together, both instruments provide excellent data for the reconstruction of the incident solar irradiance and vital information related to the determination of optical depths of water vapor, ozone, and aerosols. Other instruments used include the normal-incidence pyrheliometer and both shaded and unshaded pyranometers, which were mounted on the Kipp and Zonen's (K&Z's) two-axis positioning gear drive solar tracker, and a fixed platform. Table 1 shows a summary of the primary instruments used for this study.

For the past two years the Department of Atmospheric Sciences at UCLA has been operating an array of ground-based radiometers, including a (K&Z) CM21 pyranometer, a K&Z CG1 pyrgeometer, and an Eppley PSP. Daily solar and infrared (IR) surface downward-flux measurements by these instruments are recorded every minute and archived. In addition, a Cimel sunphotometer, CE-318, has been added to the suite of instrumentation and is a part of the NASA Goddard Space Flight Center's AERONET Program. Radiometric data collected at UCLA are employed to develop a thermal-offset correction scheme and will be utilized in a long-term study to establish the climatology of aerosol radiative forcing in the Los Angeles basin area. Figures 1(a) and 1(b) depict the arrangement of broadband radiometers and the sunphotometer, respectively. In the background of Fig. 1(a) are the short-wave radiometers mounted on the K&Z solar tracker. The cloud-screened data measured by these instruments will provide the needed surface flux to compute the SARF. Figures 1(c) and 1(d) show examples of the time series of surface downward solar and IR surface fluxes for a clear day and a partially cloudy day, respectively. Note that the direct component of the surface irradiance has not been angle corrected. The large fluctuations during the morning hours reflect the effects of clouds. The clear-sky broadband data coupled with the sunphotometer τ_a retrievals will provide for an effective assessment of the SARF.

3. Data Processing

A. Determination of Thermal Offset

Recently much attention has been given to the quantification of the thermal offset of pyranometers.[14,15] Driven by the differential heating effects of the instrument's thermopile detector, an output voltage is generated that can then be related to the radiative input via calibration. In addition to the short-wave response of the detector, there is a long-wave response due to intrinsic temperature gradients established within the device. These differences in temperature, particularly between the dome and the body of the instrument, are caused by a number of factors. For example, the small thermal conductivity of the dome causes a temperature gradient between the top and the base of the dome. The instrument is also subject to the transient conditions of the ambient air and surface temperatures as well as to the wind and precipitation.

Several approaches have been developed to characterize this effect with diffuse flux measurements. Previous studies[16–18] have shown that the observed diffuse flux density is consistently smaller than that predicted by models. One of the methods developed by Dutton *et al.*[14] is based on the relation between the pyranometer's nighttime offset and the net IR thermopile signal of a collocated pyrgeometer. We adopted this method for deriving a quantitative estimate of the pyranometer's thermal offset at the UCLA site, assuming that the pyranometer's thermal responses are approximately the same for both daytime and nighttime operations.

Both the shaded–ventilated pyranometer (K&Z CM21) and the unshaded–unventilated pyranometer (Eppley PSP) were used alongside the K&Z CG1 ventilated pyrgeometer. Two sets of nighttime data were analyzed that covered the periods of 24 May–15 June 2001 and 2 August–11 September 2001. During both periods it was found that the dark offset of both pyranometers was less than 5 W/m^2. Linear regressions were used to determine a simple function relating the PSP thermal offset to the CG1 thermopile output. Figure 2(a) shows illustrative results for the Eppley PSP during the May–June period. A

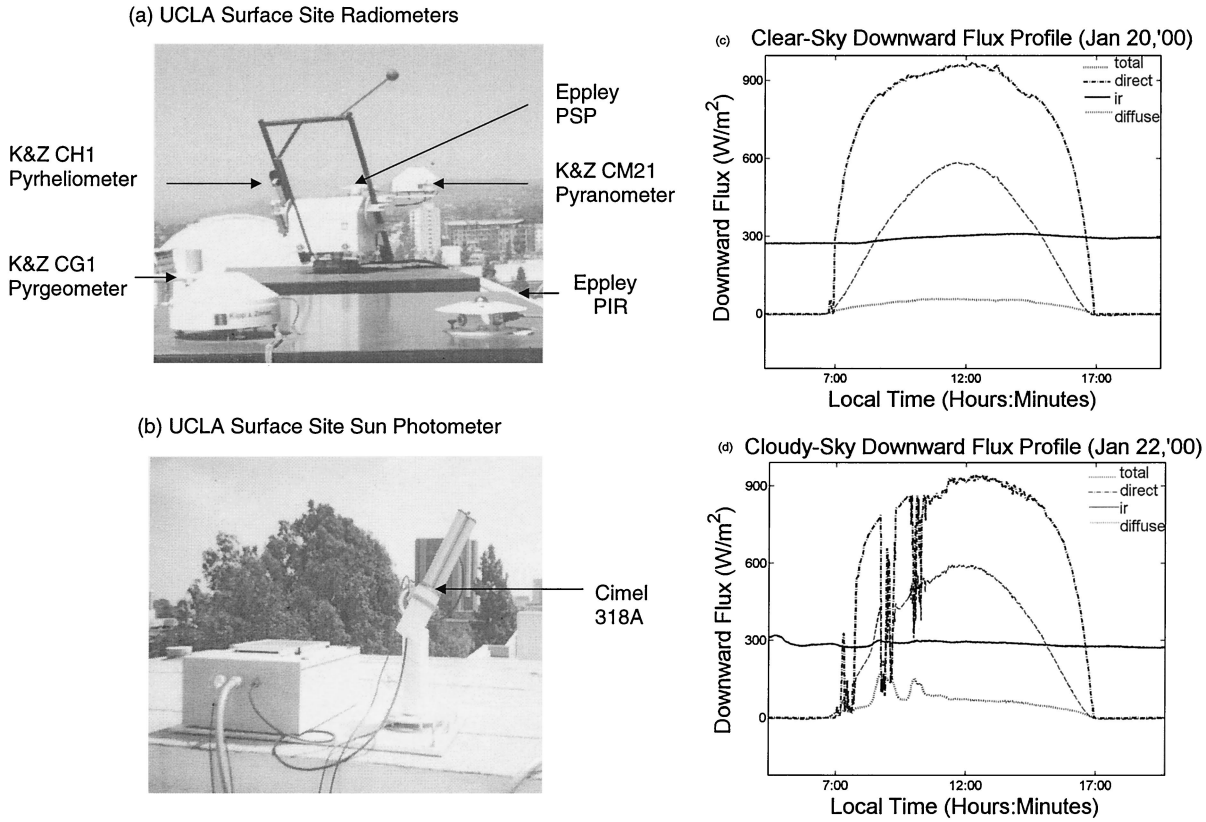

Fig. 1. (a) Arrangement of short-wave and long-wave radiometers at the UCLA surface site. (b) Cimel 318A sunphotometer at the UCLA surface radiation site. (c) Example of a downward short-wave flux profile on a clear day (20 January 2000) at the UCLA surface site. (d) Example of a downward short-wave flux profile on a partially cloudy day (22 January 2000) at the UCLA surface site.

slope of 0.039 with an intercept of −0.39 was found with the correlation coefficient of 0.9308. These regression coefficients are comparable with the slope found by Haeffelin *et al.*[15] The small slope indicates that the PSP offset is insensitive to the net IR signal. Previous studies[19] suggested that the regression be rotated around the centroid of the data to force it through the origin, so that a net IR flux of 0 W/m^2 corresponds to a zero thermal offset.

In this case, because the intercept is considered to be small enough, the use of this empirically derived relationship with a nonzero intercept is justified. The simple relationship takes the form

$$\delta^{PSP} = 0.039CG1 - 0.39, \quad (1)$$

from which the δ^{PSP}, the thermal offset, can be determined on the basis of the CG1, the thermopile output. By subtracting this offset from the irradiance measurements, one obtains a corrected signal, which is greater than the uncorrected PSP irradiances. Figure 2(b) depicts the uncorrected (range between 0 and −5 W/m^2) and corrected nighttime signals. The corrected signals are generally closer to the zero offset line than the uncorrected signals. Further thermal-offset studies involving the direct measurement of the daytime offset by one's capping the dome of the pyranometer are currently underway.

B. Cloud-Screening Procedure

Various statistical cloud-screening techniques have been developed to reduce uncertainties in retrieved aerosol optical depths from cloudy data sets.[6] The following cloud-screening technique is adopted in this study. For the same solar zenith angle, the direct component of the surface downward solar flux is generally larger for a clear atmosphere than that for a cloudy atmosphere. On the other hand, the diffuse component of the surface downward solar flux is normally smaller for a clear sky than for a cloudy sky owing to additional scattering by cloud particles. Thus we use the surface diffuse flux measured by the shaded pyranometer in conjunction with the surface direct flux measured by the normal-incidence pyrheliometer to develop a cloud-screening scheme based on their relative magnitude.

We define a parameter: the scatter ratio as the ratio of the observed diffuse flux to the observed direct flux, normalized by air mass and total irradiance. This parameter is a measure of the scattering effect of clouds. A threshold of the scatter ratio is determined by a simple approach. The time series of daily scatter ratios typically shows large scatter in the early morning and late afternoon hours with varying lower values in between. Data points associated with solar zenith angles greater than 80° were first discarded. The screening procedure then takes

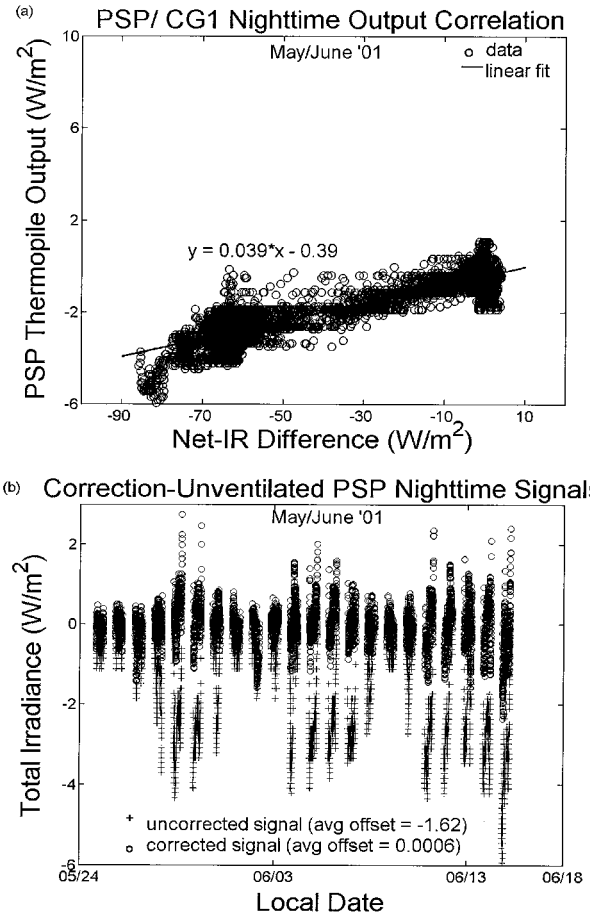

Fig. 2. (a) PSP–CG1 nighttime output correlation. (b) Correction–unventilated PSP nighttime signals.

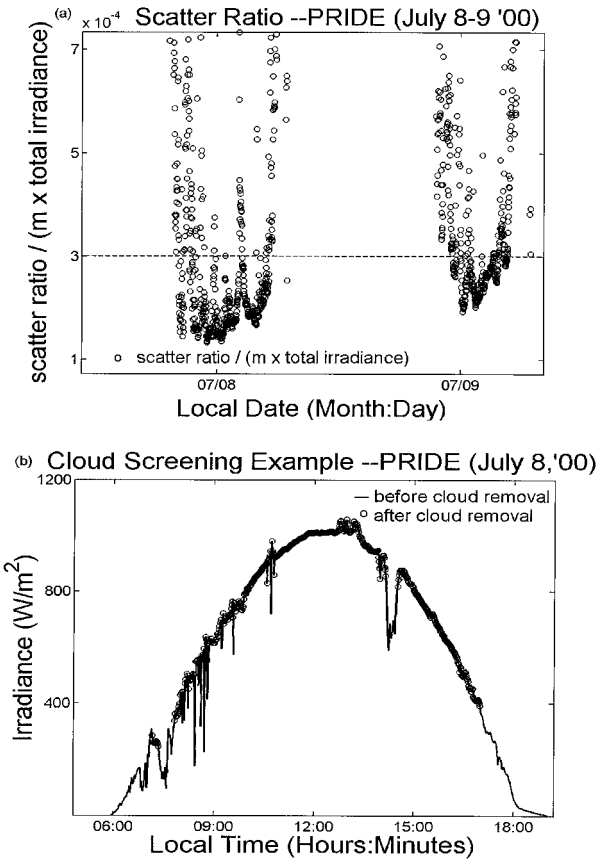

Fig. 3. (a) Scatter-ratio time series for 8 and 9 July 2000 during PRIDE. The cutoff (dashed line) is at 0.0003. (b) Comparison of total solar fluxes with and without application of the cloud-screening scheme for 8 July 2000 during PRIDE.

successive averages of the scatter ratios. During each iteration, data points greater than the average plus one standard deviation are discarded. The iteration stops when the average values converge. The final average value is taken as the threshold. An estimated threshold of 0.0003 was found for PRIDE, whereas for both SAFARI and ACE-Asia a threshold of 0.0005 was prescribed. This simple approach is similar to the clear-sky short-wave flux method used by Chou and Zhao.[20]

Figure 3(a) depicts the scatter ratios for 8 and 9 July during PRIDE. The threshold is obviously above the bulk of lower values of the scatter ratio. Points above the threshold, denoted by a dashed line, are considered to be cloud contaminated, although some of these points actually may be cloud free. For the case of a heavy Saharan Desert dust event during PRIDE, the threshold value is much higher. Figure 3(b) shows the time series of surface downward flux, measured by the TSP-700, based on filtered data, which are compared with the initial unfiltered data set for 8 July. One can see that those large drops in irradiance due to cloud contamination are removed after the screening algorithm is applied. The data at low elevation angles is also removed. This technique provides a simple means for removing cloud-contaminated data points. The computed thresholds are specified to ensure that there are enough remaining data points to produce statistically meaningful results. The YES Total Sky Imager (TSI-440) was also used as an independent check for assessing the cloud coverage. Further developments are required to make the method more robust.

C. Calibration of Irradiance from Multiple-Filter Rotating Shadowband Radiometer

For clear-sky conditions, one can perform a Langley analysis to determine the exoatmospheric solar spectral constant $I_{o\lambda}$ A linear fit of the logarithm of the direct irradiance at wavelength λ, I_λ, versus the air mass, m, yields a straight line with slope $d(\log I_\lambda)/dm$ This slope is proportional to the total optical depth of the atmospheric medium. One can further extrapolate the straight line to zero air mass to obtain the intercept, which is the exoatmospheric solar spectral irradiance constant $I_{o\lambda}$ (solar constant). The mean Earth–Sun distance must also be accounted for in computing the solar constant $I_{o\lambda}$ We assume that the total optical depth of the atmosphere does not exhibit significant temporal variations.

For cloudy-sky conditions, alternative methods in

Table 2. MFRSR Solar Spectral Constants[a]

λ (μm)	0.41	0.49	0.61	0.67	0.86	Comments
PRIDE	1.7688	2.2821	1.7715	1.6601	1.0162	Level 2 Cimel
SAFARI	1.6611	2.2088	1.6251	1.5740	0.9680	Level 1.5 Cimel
ACE-Asia	—	1.9478	1.8111	1.7323	1.1689	Level 2 Cimel
ACE-Asia	1.7674	2.1852	1.85220	1.60919	1.01072	Langley
Average	1.7324	2.1559	1.7649	1.6439	1.0409	
Standard Deviation	0.0168	0.1448	0.0989	0.0687	0.0879	
Thekaekara[22]	1.7694	1.9492	1.6185	1.4415	0.9575	1973 (Interpolated)
Neckel and Labs[23]	1.7169	1.9064	1.7140	1.5092	0.9832	1981 (Interpolated)
MODTRAN	1.6000	1.8800	1.6800	1.5400	0.9540	Version 4.0

[a]Coefficients have units of watts per square meter per nanometer.

determining the solar constant are sought. Alexandrov *et al.*[21] reviewed several retrieval algorithms for processing MFRSR data for partially cloudy conditions by using direct and diffuse measurements. The current study estimates the solar constant $I_{o\lambda}$ via two approaches. The first approach cross calibrates the MFRSR with the Cimel sunphotometer data. By use of the sunphotometer-retrieved aerosol optical depth along with the direct measurements of the MFRSR, an estimate of $I_{o\lambda}$ is obtained on the basis of the Beer–Lambert law:

$$I_\lambda / I_{o\lambda} = \exp(-\tau_t m), \quad (2)$$

where I_λ and $I_{o\lambda}$ have been defined above, τ_t is the total optical depth due to the extinction by atmospheric scattering and absorption, and m is the air mass.

The estimated accuracy by which the calibration information is transferred from the Cimel sunphotometer to the MFRSR is primarily constrained by the uncertainty in the Cimel sunphotometer τ_a retrievals as well as the reported errors in the measured spectral irradiances of the MFRSR. Initially, based on the raw data, the values obtained for $I_{o\lambda}$ varied more than expected. Values of $I_{o\lambda}$ were then calculated by use of only the filtered data, and the variation of $I_{o\lambda}$ between campaigns was reduced. As has been done with the unscreened data, a limit was imposed on $I_{o\lambda}$ to constrain the variation to no larger than a few percent. A temporal average of $I_{o\lambda}$ was then obtained from the resulting data sets for each wavelength. The second approach relies on use of the values of $I_{o\lambda}$ derived via the Langley method from the clearer days found during ACE-Asia.

Table 2 shows the resulting values of $I_{o\lambda}$ for each MFRSR channel by use of both methods in which the constant values are based on screened data only. The values of $I_{o\lambda}$ are comparable with the spectral solar constants found by Thekaekara,[22] Neckel and Labs,[23] and Anderson *et al.*[24] Cloud screening significantly improves PRIDE constants by almost 10%–15%. The solar constants from SAFARI and ACE-Asia data remain the same after screening, probably because there were not so many clouds detected as during PRIDE. The ACE-Asia 0.41-μm constant requires investigation, as it remains to be quite small. Differences in $I_{o\lambda}$ could be due to the small differences in the location in the band center of the MFRSR and Cimel sunphotometer channels (e.g., 0.41 μm versus 0.44 μm) and to the varying aerosol conditions of each field campaign.

D. Determination of Aerosol Optical Depth

Once the values of $I_{o\lambda}$ are determined, the total optical depths can be found via the Beer–Lambert law by use of the direct beam measurements of the MFRSR and the corresponding air masses. It is assumed that errors in the retrieved MFRSR τ_a are approximately linearly proportional to the uncertainties in the calibration of the MFRSR irradiance determined in Subsection 3.C. The aerosol optical depths $[\tau_a(\lambda)]$ can then be calculated for each channel by subtraction of the molecular Rayleigh scattering and ozone absorption optical depths from the total optical depth[25]:

$$\tau_a(\lambda) = 1/m(\mu_o)[\ln(I_{o\lambda}) - \ln(I_\lambda)] - \tau_R(\lambda) - \tau_o(\lambda), \quad (3)$$

where μ_o is the solar zenith angle. The data of the MFRSR 0.94-μm channel was discarded in this study so as to minimize effects of water-vapor absorption.

The parameterization of the Rayleigh scattering optical depth is expressed as follows:

$$\tau_R(\lambda) = 0.008569\lambda^{-4}(1 + 0.0113\lambda^{-2} + 0.00013\lambda^{-4})p/p_o, \quad (4)$$

where λ is the wavelength (micrometers) and p and p_o are the pressure at the observation site and standard atmospheric pressure (1013.25 mb), respectively. A corrective term to account for ozone absorption is also applied. If the column ozone amount [in Dobson units (1 DU = 10^{-3} atm cm)] is known *a priori*, its extinction optical depth can be obtained by

$$\tau_o(\lambda) = a_o(\lambda) C_o \rho, \quad (5)$$

where $a_o(\lambda)$ is the ozone absorption coefficient for wavelength λ (square centimeters per gram), C_o is the column ozone expressed in Dobson units, and ρ is the ozone number density, given by Loschmidt's number (2.69×10^{19} cm^{-3}), which is the approximate number density of particles at standard atmospheric conditions. The column ozone over the region of interest at a given time is either extracted from the NASA Total Ozone Mapping Spectrometer (TOMS) data-

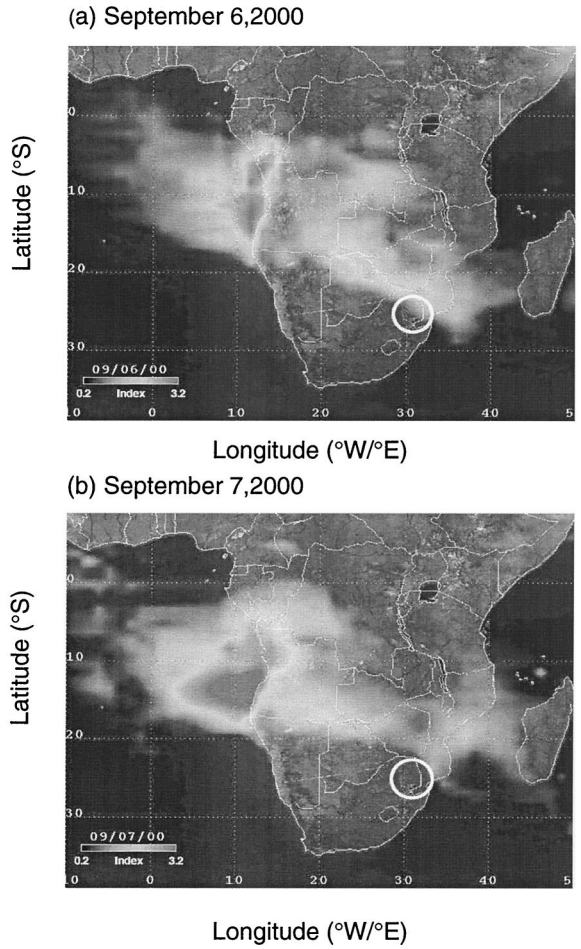

Fig. 4. (a) TOMS satellite image of the African continent on 6 September 2000 showing aerosol loading due to biomass burnings in savanna ecosystems. (b) Same as (a) except on 7 September. The circles denote the surface observation site at Skukuza, South Africa. TOMS images courtesy of Goddard Space Flight Center, NASA, Code 916.

base, as was done for this study, or calculated by the methods of Van Heuklon.[26] Alternatively, a climatological value of $C_o\rho$ can be used to determine the extinction optical depth. The absorption coefficients of other trace gases (i.e., CO2, O_2, and NO_2) in the visible spectrum are negligibly small and are therefore not considered in this study. Water-vapor absorption in the visible spectrum is also extremely small and thus neglected.

4. Observational Results

In this section we show illustrative observations and analysis results on the retrieved aerosol optical depths, turbidity coefficients, aerosol size distribution parameters, and surface aerosol radiative forcing efficiency.

A. Aerosol Optical Depth

Figures 4(a) and 4(b) show the Earth Probe TOMS satellite images of the aerosol index distribution over the African continent for 6 and 7 September 2000 during SAFARI. The aerosol index is defined as the difference between the observations and the model calculations from an aerosol-free atmosphere with the same surface reflectivity and measurement conditions. It is approximately linearly proportional to the aerosol optical depth if the index of refraction, particle size distribution, and the aerosol layer height are known from the other measurements, with the residence height as a key assumption. Information on tropospheric aerosols, which absorb ultraviolet radiation, is obtained from 0.33- and 0.36-μm radiances. The circled regions denote the geographical location of Skukuza, South Africa, where the ground-based radiometers were deployed during SAFARI. As can be seen, the aerosol loading on 6 September was much larger than on 7 September. These two images illustrate the notable change in the aerosol index from 6 to 7 September, probably owing to the large variations in the concentration of smoke particles from the local biomass burnings.

Figure 5(a) shows the ground-based cloud-screened retrieved 0.5-μm aerosol optical depth for the two dates during SAFARI. Note that both the MFRSR and the Cimel sunphotometer observed higher optical depths on 6 September than on 7 September. The retrieved MFRSR aerosol optical depths correlate well with those of the Cimel sunphotometer, with a correlation coefficient of approximately 0.93. One would think that such a high degree of correlation is expected because the instruments were cross calibrated. However, there are slight differences in the data sets that were used to derive aerosol optical depths. This could be attributed to intrinsic differences in the instruments, particularly in the central frequency of corresponding channels. Figures 5(b) and 5(c) show daily time series of retrieved aerosol optical depth for ACE-Asia and PRIDE after cloud removal, and correlation coefficients for these corresponding time series are 0.98 and 0.80, respectively. The mean and root-mean-square (rms) differences of the retrieved τ_a for both instruments during each field campaign are given in Table 3. The smallest mean difference was noted for SAFARI. Therefore this was chosen as the primary data set in subsequent analyses.

B. Aerosol Turbidity Coefficients and Shaping Factor

To infer aerosol size distributions from the sunphotometer data, we use the Angstrom empirical turbidity relation

$$\tau = \beta\lambda^{-\alpha}, \tag{6}$$

where β and α are the turbidity coefficient and the shaping factor, respectively.[25] The turbidity coefficient β is a proportionality constant relating the optical depth and the wavelength. The shaping factor α provides a measure of how rapidly aerosol optical depth (τ_a) changes with wavelength [i.e., it is a measure of the steepness of the $\log(\tau_a)$ curve versus the $\log(\lambda)$ curve]. α is also related to the size of particles. Larger particles generally correspond to smaller α,

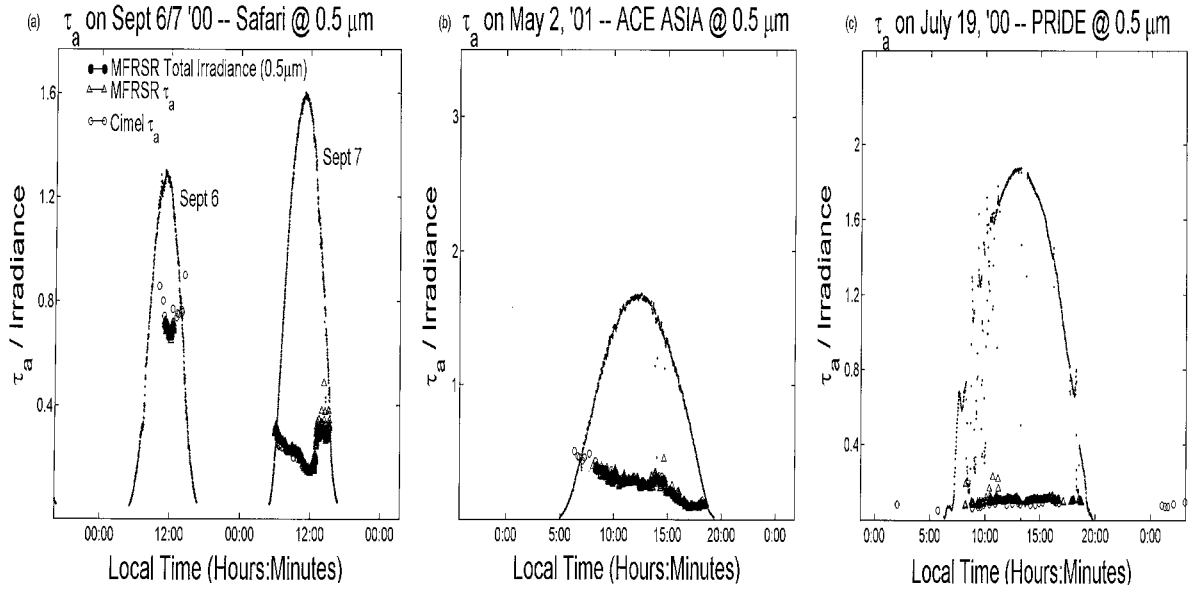

Fig. 5. (a) Retrieved 0.5-μm aerosol optical depths (Cimel sunphotometer and MFRSR) on 6 and 7 September 2000 during SAFARI. (b) Same as (a) except on 2 May 2001 during ACE-Asia. (c) Same as (a) except on 19 July 2000 during PRIDE.

whereas smaller particles generally correspond to larger α.

Plotting the logarithm of τ_a against the logarithm of the sunphotometer-channel wavelength, λ, and performing a linear regression fit of the data points in the plot would lead to a straight line with its slope and intercept corresponding to β and α, respectively. However, in this study, we adopt an alternative approach to evaluate the shaping factor α. The shaping factor can be approximated by our taking the logarithm of the ratio of Angstrom's power-law expression at two different wavelengths. If τ_a is measured at two wavelengths, then we have

$$Z = \tau_a(\lambda_1)/\tau_a(\lambda_2) = (\lambda_1/\lambda_2)^{(-\alpha+2)} = y^{(-\alpha+2)}. \quad (7)$$

Thus the shaping factor can be inferred from

$$\alpha^* = 2 - \log_y Z. \quad (8)$$

This was done by use of the wavelength pair of 0.67 and 0.86 μm for the three field campaigns as a way to understand the relative difference in the size parameters of aerosol particles for different field campaigns.

Shaping factors for both PRIDE and ACE-Asia were found to be much smaller than those for SAFARI, indicating that the size distribution of windblown dust particles over PRIDE and ACE-Asia sites are more polydispersed than that for the smoke particles over SAFARI sites. According to Eck *et al.*,[27] typical values of the shaping factor are larger than 2.0 for fresh smoke particles and close to zero for Sahelian–Saharan dust particles. Figure 6 shows the comparison of MFRSR- and Cimel sunphotometer-retrieved shaping factors from SAFARI 2000. Note the peaking shaping factors around 17 August, which are likely due to heavier loading of smoke particles than on other dates. Both data sets yield a mean coefficient of approximately 1.5. The Cimel sunphotometer data sets for PRIDE and SAFARI were evaluated for comparison. The dust studies seem to yield shaping factors in the range of approximately 0.2, whereas particles produced from biomass burnings yielded shaping factors around 1.5 and higher.

Table 3. τ_a Statistics

Campaign	R^2	Average Difference	rms Difference
PRIDE	0.80	0.016	0.004
SAFARI	0.93	0.001	0.006
ACE-Asia	0.98	0.016	0.004

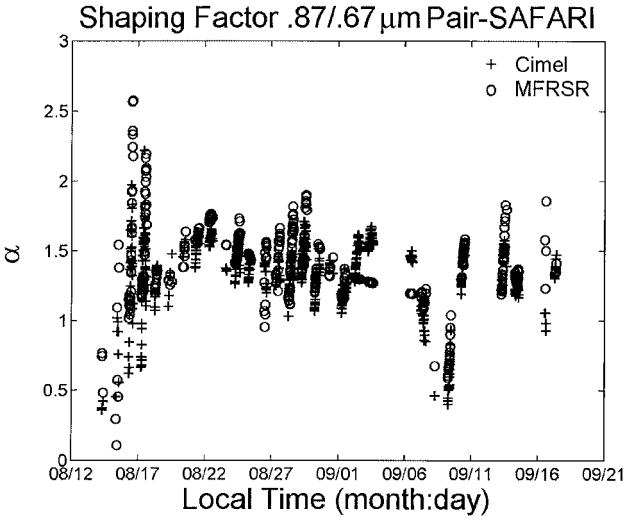

Fig. 6. Angstrom shaping factor by use of 0.87- and 0.67-μm channel pair of MFRSR and Cimel sunphotometer (SAFARI 2000).

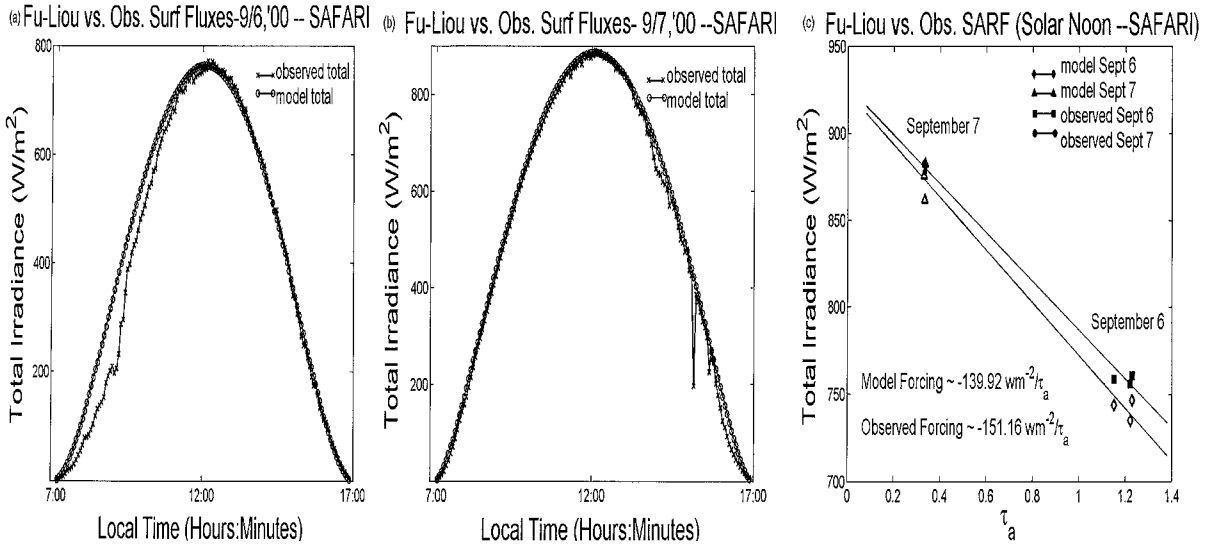

Fig. 7. (a) Results of observed surface fluxes versus Fu–Liou model on 6 September 2000 (SAFARI). (b) Results of observed surface fluxes versus Fu–Liou model on 7 September 2000 (SAFARI). (c) Results of observed SARF versus Fu–Liou model at solar noon on 6 and 7 September 2000 (SAFARI).

C. Surface Radiative Fluxes

To interpret and cross check the reliability of the observed surface radiative fluxes, we employ the one-dimensional broadband radiative transfer program developed by Fu and Liou[12] (Fu–Liou code) and later modified by Charlock and his associates. This code was chosen because of its capability to accurately simulate aerosol radiative effects through a delta-four-stream method. We use this model to compute the total, direct-normal, and diffuse surface radiative fluxes for the two chosen dates, 6 and 7 September 2000, during SAFARI. A daily average of retrieved τ_a (0.5 μm) along with the solar zenith angle was used as input to the radiative transfer code to simulate the diurnal variations of surface fluxes at Skukuza, South Africa, because both dates exhibited nearly constant values of aerosol optical depth. To obtain an approximate match of spectral bands between the YES TSP-700 pyranometer (bandwidth of 0.3–3.0 μm) and the Fu–Liou code, we compute fluxes for five of the six short-wave bands (0.2–0.7, 0.7–1.3, 1.3–1.9, 1.9–2.5, 2.5–3.5 μm) in the Fu–Liou code. Because the spectral interval of the Fu–Liou code is larger than that of the broadband radiometer (0.3–3.0 μm), the model short-wave fluxes are expected to be slightly larger than the observed surface fluxes.

Both chosen days were relatively cloud free, although a few cloudy patches were observed by use of the TSI-440 and noted. It was also difficult to assess whether subvisual cirrus clouds were present. However, in this study we prescribe the cloud optical depth to be nearly zero. A default equatorial sounding profile was used, with an assumed average surface albedo of 0.15 for the spectral range considered. Aerosol input parameters are prescribed as follows. Earlier it was shown that the aerosol loading on 6 September was heavier than on 7 September. To simulate the aerosol composition for 6 September, we assume an external mixture of 80% black carbon (soot) and 20% sulfate particles. According to Eck *et al.*,[28] 15%–20% of the aerosol produced for flaming combustion is black carbon, and less than 3% of soot is generated for smoldering combustion processes. Because the biomass burning fires in the savanna ecosystems of South Africa are of a flaming nature, the black carbon was chosen to be 20% of the total mixture of aerosols. The aerosol types and single-scattering properties are taken from the Optical Properties of Aerosols and Clouds.[29–31] The model then partitions the average optical depth according to the assumed percentages of aerosols used in the mixture.

The TOMS image for 7 September, on the other hand, shows a much smaller aerosol loading near Skukuza. For the purpose of running the model, a simple continental background aerosol that used the aerosol properties from d'Almedia *et al.*[30] was used for this date. Figures 7(a) and 7(b) show the comparison of computed surface fluxes with the observed fluxes for both dates. Figure 7(c) displays the estimated solar noontime SARF on the two days, and the difference between the calculated and the observed forcings is approximately 11 W/m^2. The differences between computed and observed fluxes shown in Fig. 7 can be explained as follows. The model computes surface fluxes under clear sky, which are compared with those observed during the cloudy periods on 6 September (morning) and on 7 September (afternoon). We have reviewed the percentage cloud cover from the TSI-440 and found that the percentage of opaque clouds in the morning of 6 September was larger than that in the afternoon of 7 September. Another possible reason for the observed discrepancy is the model's use of default equatorial temperature and pressure data. Incorporating sounding profiles obtained during the campaign into the model would most likely reduce the discrepancy. Having the

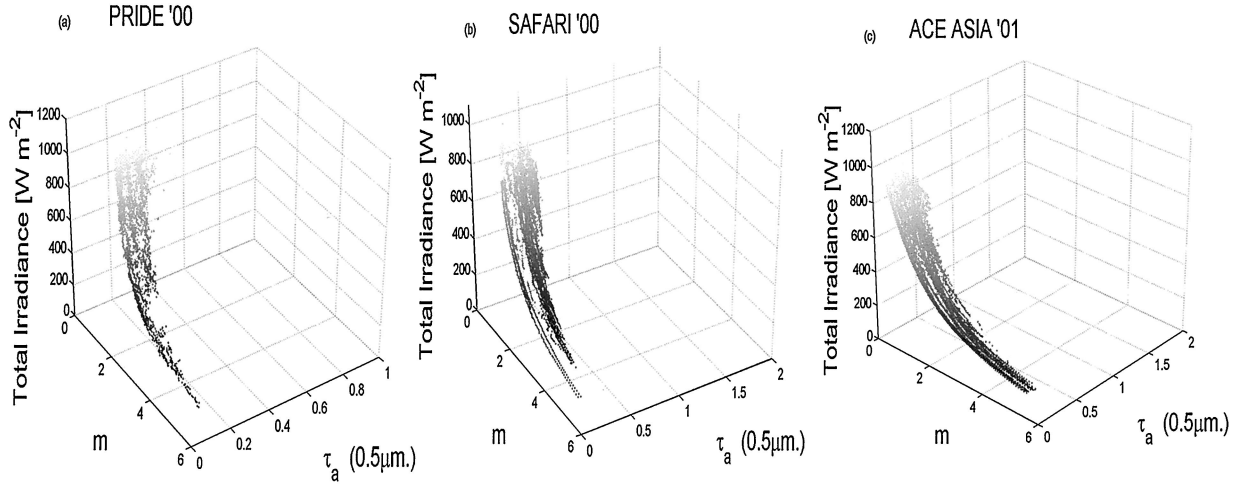

Fig. 8. (a) Estimated aerosol forcing with MFRSR-retrieved 0.5-μm aerosol optical depths (PRIDE 2000). Cloud screening applied with a scattering ratio threshold of 0.0003. (b) Estimated aerosol forcing at 0.5 μm (SAFARI 2000). Cloud screening applied with a scattering ratio threshold of 0.0005. (c) Estimated aerosol forcing at 0.5 μm (ACE-Asia 2001). Cloud screening applied with a scattering ratio threshold of 0.0005.

aerosol *in situ* data for each field campaign would also help to resolve these differences. This simple model comparison shows a reasonable agreement between predicted and observed surface fluxes in clear-sky conditions with differences less than 3%–5% for a nearly constant aerosol loading based on an aerosol composition representative of biomass burning processes. Sensitivity studies will need to be conducted to assess the impact of these variable conditions on the calculated surface fluxes.

D. Estimation of Surface Aerosol Radiative Forcing and Forcing Efficiency

Aerosol radiative forcing is defined as the difference between the observed and aerosol-free radiative fluxes. In this study we adopt the differential method to estimate the aerosol radiative forcing. Using measured surface fluxes and aerosol optical depths, we first evaluate the forcing efficiency, which is the derivative of surface flux with respect to the aerosol optical depth. By fixing an air-mass interval, the forcing efficiency over this interval can be determined by a least-squares fitting of total flux measurements versus the corresponding τ_a. We then obtain the radiative forcing by multiplying the forcing efficiency with the mean retrieved aerosol optical depth. The advantage of this method is that the aerosol radiative forcing is directly determined from observations, so that it is independent of assumptions made on the aerosol single-scattering properties.

Three-dimensional surface plots were generated for data obtained during each campaign. With reference to Figs. 8(a)–8(c) the data are expressed in terms of three variables, τ_a, air mass (m), and total surface flux. The total surface flux was measured by either the TSP or PSP. The resulting surface plots allow the visual determination of the radiative forcing efficiency for different intervals of air mass. For a fixed interval of air mass, the steeper the surface is, the larger the aerosol forcing efficiency. Figures 9(a)–9(b) depict the air-mass-dependent radiative forcing efficiencies for PRIDE, SAFARI, and ACE-Asia, respectively. Note that the total number of data points for PRIDE is less because the PRIDE data-collecting period was shorter than the other campaigns by approximately two weeks. Linear regressions were applied to data points for each air-mass interval, and the slope ($dF/d\tau_a$) for each fitted straight line corresponds to the forcing efficiency. The slopes depicted also represent maximum correlation between the total irradiance and the aerosol optical depth. Figure 9(a) shows that there was considerable scatter in the data, probably because the MFRSR's shadowband does not completely cover the sensor during diffuse radiometric measurements and sea salt built up on the dome of the radiometer.

Compared with Ji's initial solar noon radiative forcing efficiency $[-95\ (\mathrm{W/m^2})/\tau_a]$ based on the Cimel sunphotometer data from PRIDE, the MFRSR-derived efficiency is higher by approximately 25–50 $(\mathrm{W/m^2})/\tau_a$ as shown in Fig. 8(a) and 9(a). The radiative forcing efficiency first decreases with increasing air mass up to $\theta_o = 60°$, then increases again. For air masses larger than 3, the estimated radiative forcing results are subject to large uncertainties because of fewer data points in those intervals. The mean τ_a at 0.5 μm observed during PRIDE was found to be 0.21 for the MFRSR and 0.24 for the Cimel sunphotometer. The estimated radiative forcings for air masses of 1.5 and 2.0 were found to be -12.82 and $-19.68\ \mathrm{W/m^2}$, respectively. Christopher *et al.*[5] used aerosol optical depth retrievals from half-hourly GOES-8 imager data along with the measured downward solar flux by use of the NASA Surface Measurements for Atmospheric Radiative Transfer platform to derive a quantitative estimate of the radiative forcing due to dust at both the surface and the top of the atmosphere. Surface radiative forcings at approxi-

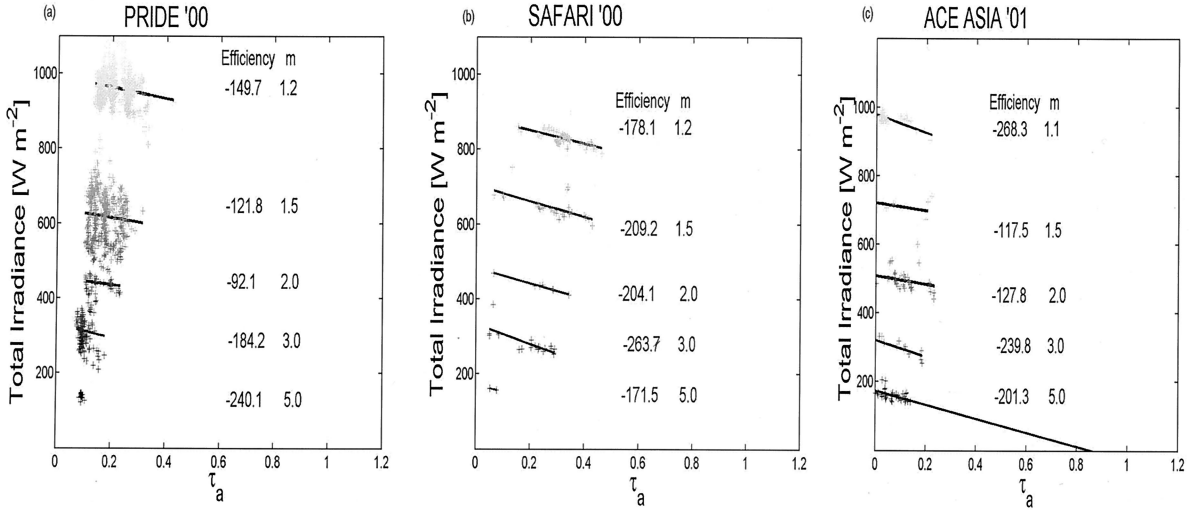

Fig. 9. (a) Estimated forcing efficiency at 0.5 μm with slices of air mass of 1.2, 1.5, 2.0, 3.0, and 5.0. (b) Estimated forcing efficiency at 0.5 μm with slices of air mass of 1.2, 1.5, 2.0, 3.0, and 5.0. (c) Estimated forcing efficiency at 0.5 μm with slices of air mass of 1.1, 1.5, 2.0, 3.0, and 5.0.

mate air masses of 1.5 and 2.0 were found to be -19.66 ± 16.71 and -20.36 ± 16.92 W/m^2, respectively. These ranges of satellite-derived radiative forcings compare well with the results from the present study.

For SAFARI, as shown in Figs. 8(b) and 9(b), after several outliers for large air mass and large τ_a are discarded, the radiative forcing efficiencies are much higher than those for PRIDE. This could be attributed to the large amount of absorbing aerosols emitted from the local biomass burnings at Skukuza. The surface plot found in Fig. 8(c) is from ACE-Asia. For most of the time the Sun remained low in the sky. The smallest air mass observed was around 1.1 on 9 May, corresponding to $\theta_o = 70°$. The observed radiative forcing efficiencies are comparable but slightly higher than PRIDE and could be due to the effect of urbanized aerosols detected during ACE-Asia. This might be consistent, perhaps, with the dust aerosols observed for both field campaigns. Further research is required to reduce the uncertainties in the PRIDE data and to make physically more meaningful comparisons to other studies done that used both ground- and satellite-based platforms.

5. Summary

Surface aerosol radiative forcing parameters have been determined by use of spectral and radiometric data obtained during PRIDE 2000, SAFARI 2000, and ACE-Asia 2001. A brief introduction of the UCLA radiometric surface site along with a description of the measured data and current research plans was presented. To remove cloud contamination, we employed a cloud-screening filter to reject data points with scatter ratios larger than an empirically determined threshold. We anticipate constructing a more robust physically based method in the future. A thermal-offset correction procedure was also used to account for the differential heating effects of the pyranometer.

Through a cross-calibration scheme and the Beer–Lambert law, aerosol optical depths were retrieved from the MFRSR data sets and compared with those obtained from the Cimel sunphotometer. A correlation coefficient of approximately 93% was obtained. Errors in the calibration transfer are constrained by the uncertainty in the Cimel sunphotometer τ_a retrievals as well as the reported errors in the measured spectral irradiances of the MFRSR. The Angstrom shaping factor was also determined with focus on the SAFARI campaign. We found a mean value of 1.5 by employing a simple wavelength-pairing technique using Beer's law. Coefficients found from PRIDE and ACE-Asia were smaller, indicating larger-size particles, which could be due to desert dust aerosols. To interpret and cross check the measured radiative fluxes, we used the Fu–Liou radiative transfer code to calculate the total downwelling surface fluxes and hence the forcing corresponding to the conditions found during SAFARI. Surface radiative fluxes were computed by use of a nearly constant observed aerosol optical depth and solar zenith angles corresponding to Skukuza, South Africa, over a two-day period. The predicted surface fluxes are within 3%–5% of the measured fluxes. The estimated noontime forcing efficiencies for these two days were found to be around -139.92 (W/m^2)/τ_a compared with the observed value of -151.16 (W/m^2)/τ_a with a difference of 11.2 (W/m^2)/τ_a.

The retrieved aerosol optical depths were then used along with the total surface flux measurements to derive the forcing efficiencies for different air-mass intervals on the basis of linear least-squares fitting. The larger efficiencies found for SAFARI [~ -176.0(W/m^2)/τ_a] and ACE-Asia [~ -286.0 (W/m^2)/τ_a] are most likely due to the highly absorbing aerosols generated from local biomass burnings, biological and industrial sources, and urbanized sources. For air-mass intervals of 1.5 and 2.0, and by use of an averaged τ_a of 0.21,

the calculated SARF for PRIDE was found to be -12.82 and -19.68 W/m^2, respectively.

Further investigation is required in SARF studies, particularly in the areas of cloud-removal schemes, and comparisons of SARF with computations. Measured aerosol optical properties, cloud information, and meteorological sounding data will be used to accurately assess the model's performance with the observed quantities. We anticipate that the current study will provide for and encourage alternative strategies in the estimation of SARF over various regions with variable aerosol composition.

This research has been supported in part by National Science Foundation grant ATM-99-07924, NASA grant NAG5-7738, and Department of Energy grant DE-FG03-00ERG2904. The sunphotometer data have been provided by the AERONET program manager.

References

1. B. N. Holben, T. F. Eck, I. Slutsker, D. Tanre, J. P. Buis, A. Setzer, E. Vermote, J. A. Reagan, Y. K. Kaufman, T. Nakajima, F. Lavenu, I. Jankowiak, and A. Smirnov, "AERONET—a federated instrument network and data archive for aerosol characterization," Remote Sens. Environ. **66,** 1–16 (1998).
2. T. Nakajima, M. Tanaka, and T. Yamauchi, "Retrieval of the optical properties of aerosols from aureole and extinction data," Appl. Opt. **22,** 2951–2959 (1983).
3. O. Dubovik and M. D. King, "A flexible inversion algorithm for retrieval of aerosol optical properties from sun and sky radiance measurements," J. Geophys. Res. **105,** 20673–20696 (2000).
4. J. S. Schafer, T. F. Eck, B. N. Holben, P. Artaxo, M. A. Yamasoe, and A. S. Procopio, "Observed reductions of total solar irradiance by biomass burning aerosols in the Brazilian Amazon and Zambian Savanna," Geophys. Res. Lett. **29,** 1823–1826 (2002).
5. S. A. Christopher, J. Wang, Q. Ji, and S. C. Tsay, "Estimation of diurnal shortwave dust aerosol radiative forcing during PRIDE," J. Geophys. Res. **108,** 8596–8607 (2003).
6. W. C. Conant, "An observational approach for determining aerosol surface radiative forcing: results from the first field phase of INDOEX," J. Geophys. Res. **105,** 15347–15360 (2000).
7. J. Meywerk and V. Ramanathan, "Observations of the spectral clear-sky aerosol forcing over the tropical Indian Ocean," J. Geophys. Res. **104,** 24359–24370 (1999).
8. T. F. Eck, B. N. Holben, D. E. Ward, M. M. Mukelabai, O. Dubovik, A. Smirnov, J. S. Schafer, N. C. Hsu, S. J. Piketh, A. Queface, J. Le Roux, R. J. Swap, and I. Slutsker, "Variability of biomass burning aerosol optical characteristics in southern Africa during the SAFARI 2000 dry season campaign and a comparison of single scattering albedo estimates from radiometric measurements," J. Geophys. Res. **108,** 8477–8497 (2003).
9. J. Redemann, S. Masonis, B. Schmid, T. Anderson, P. Russell, J. Livingston, O. Dubovik, and A. Clarke, "Clear-column closure studies of aerosols and water vapor aboard the NCAR C-130 in ACE-Asia, 2001," J. Geophys. Res., submitted for publication.
10. J. A. Augustine and C. I. Medina, "A new automated method of MFRSR-based optical depth analysis," presented at the Twelfth Symposium on Meteorological Observations and Instrumentation, Long Beach, Calif., 9–13 February 2003.
11. Z. Jin, T. Charlock, and K. Rutledge, "Analysis of broadband solar radiation and albedo over the ocean surface at COVE," J. Atmos. Oceanic Technol. **19,** 1585–1601 (2002).
12. Q. Fu and K. N. Liou, "On the correlated k-distribution method for radiative transfer in nonhomogeneous atmospheres," J. Atmos. Sci. **49,** 2139–2156 (1992).
13. Atmospheric Radiation Measurement web site (http://www.arm.gov/docs/instruments/static/mfrsr.html).
14. E. G. Dutton, J. J. Michalsky, T. Stoffel, B. W. Forgan, J. Hickey, D. W. Nelson, T. L. Alberta, and I. Reda, "Measurement of broadband diffuse solar irradiance using current commerical instrumentation with a correction for thermal offset errors," J. Atmos. Oceanic. Technol. **18,** 297–314 (2001).
15. M. Haeffelin, S. Kato, A. M. Smith, C. K. Rutledge, T. P. Charlock, and J. R. Mahan, "Determination of the thermal offset of the Eppley precision spectral pyranometer," Appl. Opt. **40,** 472–484 (2001).
16. T. P. Charlock and T. L. Alberta, "The CERES/ARM/GEWEX Experiment (CAGEX) for the retrieval of radiative fluxes with satellite data," Bull. Am. Meteorol. Soc. **77,** 2673–2683 (1996).
17. S. Kato, T. P. Ackerman, E. E. Clothiaux, J. H. Mather, G. G. Mace, M. L. Wesely, F. Murcray, J. Michalsky, "Uncertainties in modeled and measured clear-sky surface shortwave irradiances," J. Geophys. Res. **102,** 25882–25898 (1997).
18. R. N. Halthore, S. E. Schwartz, J. J. Michalsky, G. P. Anderson, R. A. Ferrare, B. N. Holben, H. Ten Brink, "Comparison of model estimated and measured direct-normal solar irradiance," J. Geophys. Res. **102,** 22991–20002 (1997).
19. T. L. Alberta and T. P. Charlock, "A comprehensive resource for the investigation of shortwave fluxes in clear conditions: CAGEX version 3," in preprints of the Tenth Conference on Atmospheric Radiation (American Meteorological Society, Boston, Mass., 1999), pp. 279–282.
20. M. D. Chou and W. Zhao, "Estimation and model validation of surface solar radiation and cloud radiative forcing using TOGA COARE measurements," J. Clim. **10,** 610–620 (1997).
21. M. D. Alexandrov, A. A. Lacis, B. E. Carlson, and B. Cairns, "Remote sensing of atmospheric aerosols and trace gases by means of multifilter rotating shadowband radiometer. Part I: retrieval algorithm," J. Atmos. Sci. **59,** 524–543 (2001).
22. M. P. Thekaekara, "Extraterrestrial solar spectrum, 3000–6100 Å at 1-Å intervals," Appl. Opt. **13,** 518–522 (1974).
23. H. Neckel and D. Labs, "Improved data of solar spectral irradiance from 0.33 to 1.25 μm," Sol. Phys. **74,** 231–249 (1981).
24. G. P. Anderson, R. H. Picard, and J. H. Chetwynd, eds., *Proceedings of the Seventeenth Annual Review Conference on Atmospheric Transmission Models*, PL/TR-95-2060, Special Report No. 274 (Air Force Research Laboratory/VSBT, Hanscom Air Force Base, Mass., 1995).
25. K. N. Liou, *An Introduction to Atmospheric Radiation*, 2nd ed. (Academic, San Diego, Calif., 2002).
26. T. K. Van Heuklon, "Estimating atmospheric ozone for solar radiation models," Sol. Energy **22,** 63–68 (1979).
27. T. F. Eck, B. N. Holben, J. S. Reid, O. Dubovik, A. Smirnovm, N. T. O'Neill, I. Slutsker, and S. Kinne, "An observational approach for determining aerosol surface radiative forcing: results from the first field phase of INDOEX," J. Geophys. Res. **105,** 15347–15360 (2000).
28. T. F. Eck, B. N. Holben, D. E. Ward, O. Dubovik, J. S. Reid, A. Smirnov, M. M. Mukelabai, N. C. Hsu, N. T. O'Neill, and I. Slutsker, "Characterization of the optical properties of biomass burning aerosols in Zambia during the 1997 ZIBBEE field campaign," J. Geophys. Res. **106,** 3425–3448 (2001).
29. M. Hess, P. Koepke, and I. Schult, "Optical properties of aerosols and clouds: the software package OPAC," Bull. Am. Meteorol. Soc. **79,** 831–844 (1998).
30. G. d'Almedia, P. Koepke, and E. P. Shettle, *Atmospheric Aerosols: Global Climatology and Radiative Characteristics* (Deepak, Hampton, Va., 1999).
31. I. Tegen and A. A. Lacis, "Modeling of particle size distribution and its influence on the radiative properties of mineral dust aerosol." J. Geophys. Res. **101,** 19237–19244 (1996).